Enhanced Working Voltage in Hydrated Vanadate Cathodes: Insights into [VO$_6$] Octahedral Distortion and V 3d Orbital Splitting

Huanhuan Niu, Heng Liu, Wei-Hsiang Huang, Ting Shen, Menghao Yang, Min-Hsin Yeh, Long Yang,* and Chaofeng Liu*

The bi-layered hydrated vanadate is anticipated as a promising next-generation cathode material for high-energy zinc-ion batteries. However, the practical application has been impeded by undesirable voltage fade, which originates from local structure distortion induced by zinc ion (de)intercalation. Herein, V$_2$O$_5$·nH$_2$O pre-intercalated with various organic cations is investigated to elucidate the relationship between electronic structure modulation and voltage variations during local structure evolution. Microscopic scale observations—using ex situ X-ray diffraction, synchrotron X-ray pair distribution function along with X-ray absorption fine structure spectroscopy—reveal that the electronic structure perturbation is governed by the distortion of [VO$_6$] octahedra, which leads to V 3d orbitals splitting. Specifically, the structural distortion induces variations in vanadium-oxygen bond lengths and alters the ligand-field electronic structure, boosting the operating voltage (44 mV higher midpoint voltage) and cycling stability (91.3% retention after 3000 cycles). These findings reveal a fundamental correlation for the development of high-energy-density batteries with superior stability through local structural design.

1. Introduction

Developing safe, cost-effective, and sustainable energy storage systems is crucial to meet grid-scale energy storage demands, particularly for integrating intermittent renewables like solar and wind energy.[1–3] Rechargeable batteries, which store energy through redox reactions of electrode materials that accommodate working ions within their crystal lattice and electrons in orbitals, offer high energy density, efficiency, and environmental sustainability.[4,5] The increasing demands for high-energy-density batteries have driven the exploration of advanced cathode materials featuring both high voltage output and large specific capacity.[6,7] Among various candidates, bi-layered hydrated vanadate, such as V$_2$O$_5$·nH$_2$O (denoted as VOH), has attracted significant attention as a promising cathode for secondary batteries, because of its unique layered structure that can host a variety of working ions.[8–11] Moreover, due to its variable chemical valence of vanadium (V) from 3$^+$ to 5$^+$, hydrated vanadate offers high theoretical capacity exceeding 580 mA h g^{-1}.[12] However, practical applications of this material are still hindered by its low electrochemical kinetics and significant capacity fading upon long-term cycling.[13]

For boosting the electrochemical kinetics and stability, pre-intercalation of guest species into the interlayer space has emerged as a feasible and effective approach.[8,14–17] For example, interlayer water molecules enhance ion diffusion kinetics and cycling stability by expanding interlayer spacing and forming hydrogen bonds within the host framework.[18] The intercalation of inorganic cations can form rigid chemical bonds with oxygen atoms and suppress structural collapse during cycling.[19,20] The intercalated electroneutral flexible organic molecule mitigates lattice strain during charge/discharge and shields the positive charge of working ions.[21] Recently, the incorporation of organic cations, which combine the properties of inorganic cations and organic molecules,[22] exhibits strong electrostatic interactions with the [VO] skeleton and alleviates lattice strain due to the flexibility of organics, enabling a robust crystal structure.[23,24] However, the fundamental mechanisms underlying the pre-intercalation-induced structural perturbations in the V 3d

H. Niu, H. Liu, M. Yang, L. Yang, C. Liu
Interdisciplinary Materials Research Center
School of Materials Science and Engineering
Tongji University
Shanghai 201804, China
E-mail: long_yang@tongji.edu.cn; chaofeng@tongji.edu.cn

W.-H. Huang
National Synchrotron Radiation Research Center (NSRRC)
Hsinchu 30076, Taiwan

W.-H. Huang, M.-H. Yeh
Sustainable Electrochemical Energy Development (SEED) Center
National Taiwan University of Science and Technology
Taipei 106, Taiwan

T. Shen
Department of Materials Science and Engineering
Clemson University
Clemson, SC 29634, USA

M.-H. Yeh
Department of Chemical Engineering
National Taiwan University of Science and Technology
Taipei 10607, Taiwan

**ADVANCED
SCIENCE NEWS**

www.advancedsciencenews.com

**ADVANCED
FUNCTIONAL
MATERIALS**

www.afm-journal.de

orbitals and electronic structure of hydrated vanadate remain poorly understood. In particular, the specific contributions to enhance the working voltage and cycling stability require further investigation.

In this study, we demonstrate that the distinct coordination environments of V cations can trigger a realignment of the electronic structure at redox-active sites, thereby achieving enhanced working voltage and cycling stability. The detailed structural distortions of $[VO_6]$ octahedra were investigated through X-ray absorption fine structure (XAFS) spectroscopy and synchrotron X-ray atomic pair distribution function (PDF) analysis. Compared to the sample (denoted as ChVOH) with pre-inserted choline cation ($C_5H_{13}N^+OH$), the expanded $[VO_6]$ octahedra units in the sample (denoted as βVOH) of pre-inserted by β-choline cation ($C_6H_{15}N^+OH$) lead to reduced energy levels of redox V $3d$ orbitals. βVOH demonstrates elevated midpoint and working voltages along with superior cycling stability. Furthermore, density functional theory (DFT) calculations were conducted to systematically investigate its d-band and crystal structure evolution. This study not only provides theoretical guidance for the rational design of electrode materials but also establishes fundamental mechanistic insights into atomic-scale strategies for optimizing electronic structure in functional materials.

2. Results and Discussion

2.1. Structural Information and Chemical States

The samples were synthesized via pre-intercalation of $C_5H_{13}N^+OH$ and $C_6H_{15}N^+OH$, with experimental details provided in the Supporting Information. Fourier transform infrared (FTIR) spectra in **Figure 1**a and its enlarged part in Figure 1b reveal the peaks near 740 and 1005 cm^{-1} represent the characteristic bands of the vanadium oxide framework.[25] The peaks $\approx$740 cm^{-1} associate with the stretching vibration of V—O—V bonds, while the peaks $\approx$1005 cm^{-1} correspond to V=O stretching vibrations.[26,27] The in-plane bending vibration of C—H is detected at 1463 cm^{-1} in both samples (Figure 1c), which is attributed to the methyl and methylene C—H bonds from pre-intercalated organic cations.[28] The peaks are located near 1622 cm^{-1} of both samples corresponds to the bending vibration of H—O—H,[29] indicating both samples contain a small amount of interlayer or adsorbed water molecules. The X-ray diffraction (XRD) patterns in Figure 1d and the high-resolution transmission electron microscopy (HR-TEM) analysis (Figure S1, Supporting Information) collectively reveal that both ChVOH and βVOH exhibit distinct (001) interplanar distances of 12.9 and 12.7 Å, respectively. The Raman spectra in Figure 1e exhibit four characteristic vibrational modes at $\approx$700, 516, 400, and 280 cm^{-1} in both samples. These spectral features can be attributed to distinct V—O bonding. The higher frequency modes at 516 and 700 cm^{-1} correspond to the symmetric and asymmetric stretching vibrations of V—O bonds, respectively. The lower frequency bands at 400 and 280 cm^{-1} originate from the bending vibrational modes of the V=O functional groups.[30] The X-ray photoelectron spectroscopy (XPS) spectra in Figure 1f exhibit five distinct characteristic peaks corresponding to the V 2s, O 1s, V 2p, N 1s, and C 1s, respectively. In the V 2p high-resolution spectra (Figure 1g), two pairs of spin-orbit splitting peaks

are observed within the binding energy range of 513–527 eV, which correspond to the V^{4+} and V^{5+} oxidation states.[31,32] The emergence of the V^{4+} component predominantly originates from the charge compensation mechanism induced by pre-intercalated cations, which effectively reduces the proportion of V^{5+} for electroneutrality. The peak area of V^{4+} in ChVOH is marginally greater compared to that in βVOH, indicative of a marginally higher concentration of pre-intercalated cations within the ChVOH structure. This observation aligns with the enhanced paramagnetic signal intensity detected through electron paramagnetic resonance (EPR) spectroscopy (Figure S2, Supporting Information). In the high-resolution N 1s XPS spectra (Figure 1h), two distinct peaks at 399.2 and 399.3 eV are assigned to the C—N bonding in pre-intercalated organic cations. A prominent peak observed at 401.5 or 401.1 eV can be attributed to N—O bonding interactions formed through coordination between $C_5H_{13}N^+OH$ or $C_6H_{15}N^+OH$ and oxygen atoms within the host lattices.[33] The corresponding O 1s spectra (Figure 1i) reveal three characteristic components in the 526–534 eV range for both samples, corresponding to V—O, C—O bonds, and intercalated water molecules.[21] Thermogravimetric analysis coupled with differential scanning calorimetry (TG-DSC, Figure S3, Supporting Information) quantitatively determined the organic cation content as 5.8 and 6.4 wt.% for βVOH and ChVOH, respectively. Both samples exhibit significant interlayer water content, with βVOH and ChVOH showing 8.1 and 7.6 wt.% weight loss, respectively, during the removal of lattice water processes.

2.2. Coordination Structure of Vanadium Cation

Synchrotron X-ray atomic PDF analysis was conducted to investigate detailed bond length characteristics.[34,35] The PDF local structure analysis confirms the presence of local structural distortions in ChVOH and βVOH, as evidenced by local structural refinements presented in **Figure 2**a,b. The detailed PDF results are listed in Tables S1–S3 (Supporting Information). The PDF profiles reveal distinct differences in the local coordination environments between the two samples. The refined structure model (Figure S4, Supporting Information) features four oxygen atoms, located at distances ranging from 1.79 to 2.10 Å, that form a plane with the V atom, while oxygen atoms are positioned $\approx$1.60 Å above and $\approx$2.50 Å below this plane. The positions of PDF peaks correspond directly to the real-space bond lengths. Details of atomic X-ray PDF data processing and local structural analysis can be found in previous work.[22,36–39] Through quantitative local structural modeling against the experimental PDF data, the distinct effects of bond-length variations on characteristic PDF features can be systematically resolved. The peaks at 1.8 and 2.4 Å (Figure 2c) are assigned to the V—O bonds. The peak at 3.0 Å is mainly from the nearest V—V bonds, with a minor contribution from O—O bonds. The 3.6 Å peak mostly originates from V—V pairs along the a and b crystallographic axes. These V cations form the motif of the octahedra layer. Notably, the PDF analysis reveals that the position of the 3.6 Å peak remains nearly unchanged, suggesting the interlayer structural skeleton is preserved in both materials. Therefore, PDF analysis indicates that
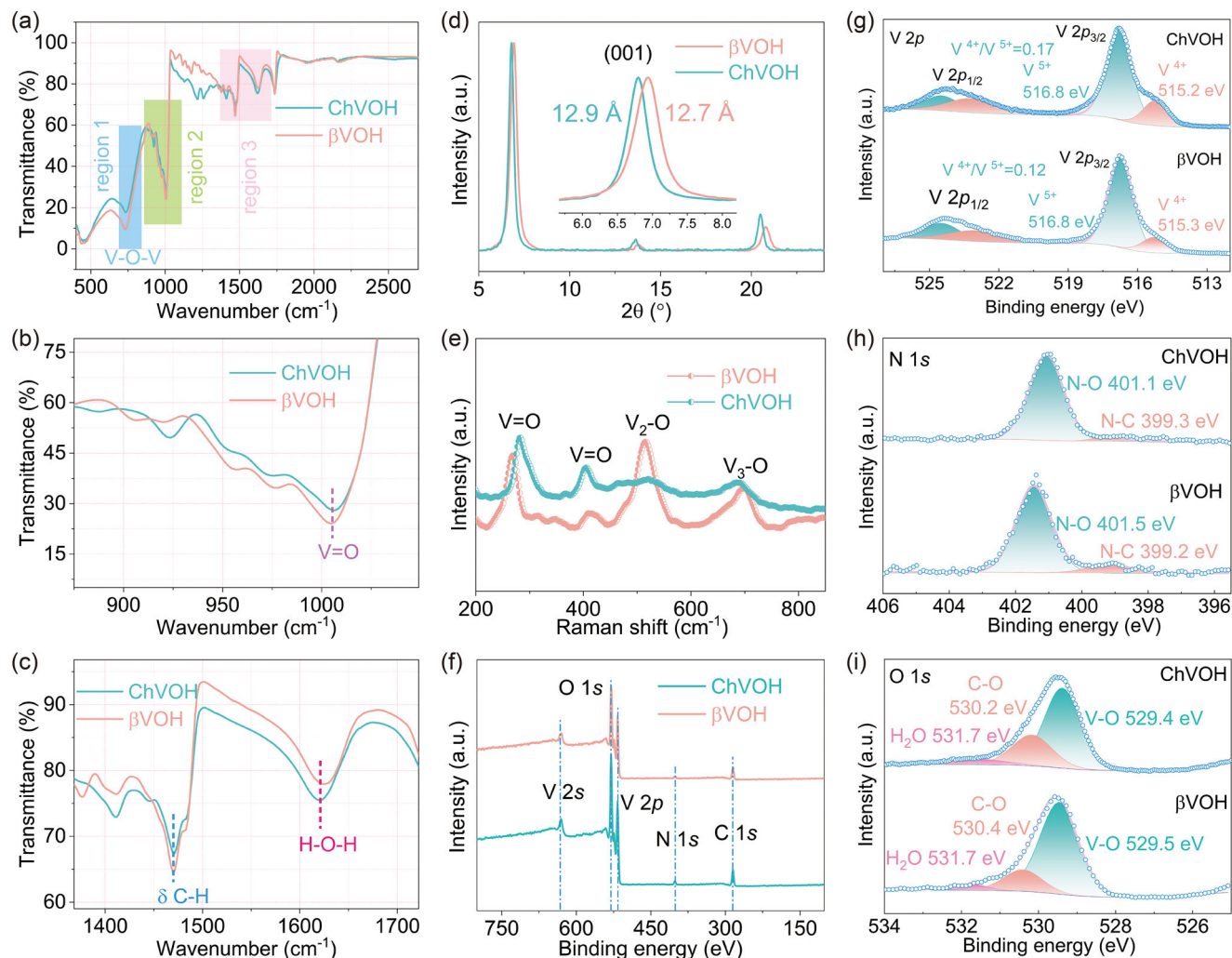
Figure 1. Structure information and chemical states of ChVOH and βVOH. a) FTIR spectra. b) Enlarged image of region 1 from FTIR spectra exhibits $V^{4+} = O$ and $V^{5+} = O$ vibration. c) Enlarged image of region 2 from FTIR spectra. It exhibits the vibrations of δ-C—H and H—O—H. d) XRD patterns. Both samples have the same crystal structure but different spacing distances. e) Raman spectra. f) XPS survey spectra. g) High resolution V 2p XPS spectra. Intercalated organics introduce V^{4+} in both lattices for electroneutrality, confirming the successful pre-intercalation. h) High-resolution XPS spectra of N 1s. The presence of C—N bonds originates from the skeletons of organic cations, and the formation of N—O bonds suggests the chemical interaction between the intercalants and the lattice oxygen. i) High resolution O 1s XPS spectra.

the changes on the O atom sites are the primary cause of the structural distortions in ChVOH and βVOH.

XAFS spectroscopy was performed to further analyze the coordination environment[40] and structural geometry of both samples (Figure 2d,e). The V K-pre-edge peak at $\approx$5471 eV consists of weak transitions that are electric dipole-forbidden but quadrupole-allowed, involving 1s core electrons transitioning into valence 3d orbitals, demonstrating high sensitivity to crystal field symmetry and electron occupancy of V 3d orbitals.[41] According to the selection rules governing electric dipole transitions, the electronic transitions of 1s→3d should theoretically be prohibited. Nevertheless, the pronounced pre-edge features are experimentally observed in both samples, providing direct spectroscopic evidence for significant orbital hybridization occurring between O 2p and V 3d orbitals.[42] The enhanced pre-edge peak intensity observed in βVOH relative to ChVOH implies an in-

creased population of unoccupied V 3d orbitals.[43] Notably, the near-edge region of ChVOH demonstrates a characteristic low-energy shift compared to βVOH, suggesting a marginally reduced vanadium oxidation state in the former material. Figure 2b presents the K^2-weighted Fourier transforms derived from V K-edge extended X-ray absorption fine structure (EXAFS) spectra, along with their corresponding Artemis simulated fitting curves for both samples.[44] The radial distribution function associated with the absorption features of V atoms demonstrates significant variations in local structure. Both samples were analyzed in R-space using identical crystalline structural parameters for fitting (Figure S4, Supporting Information), without phase correction in the refinement process. Pre-inserted organic cations induce lattice distortion through increased interlayer spacing, consequently altering the distance between V and O coordination shells. This structural modification accounts for the
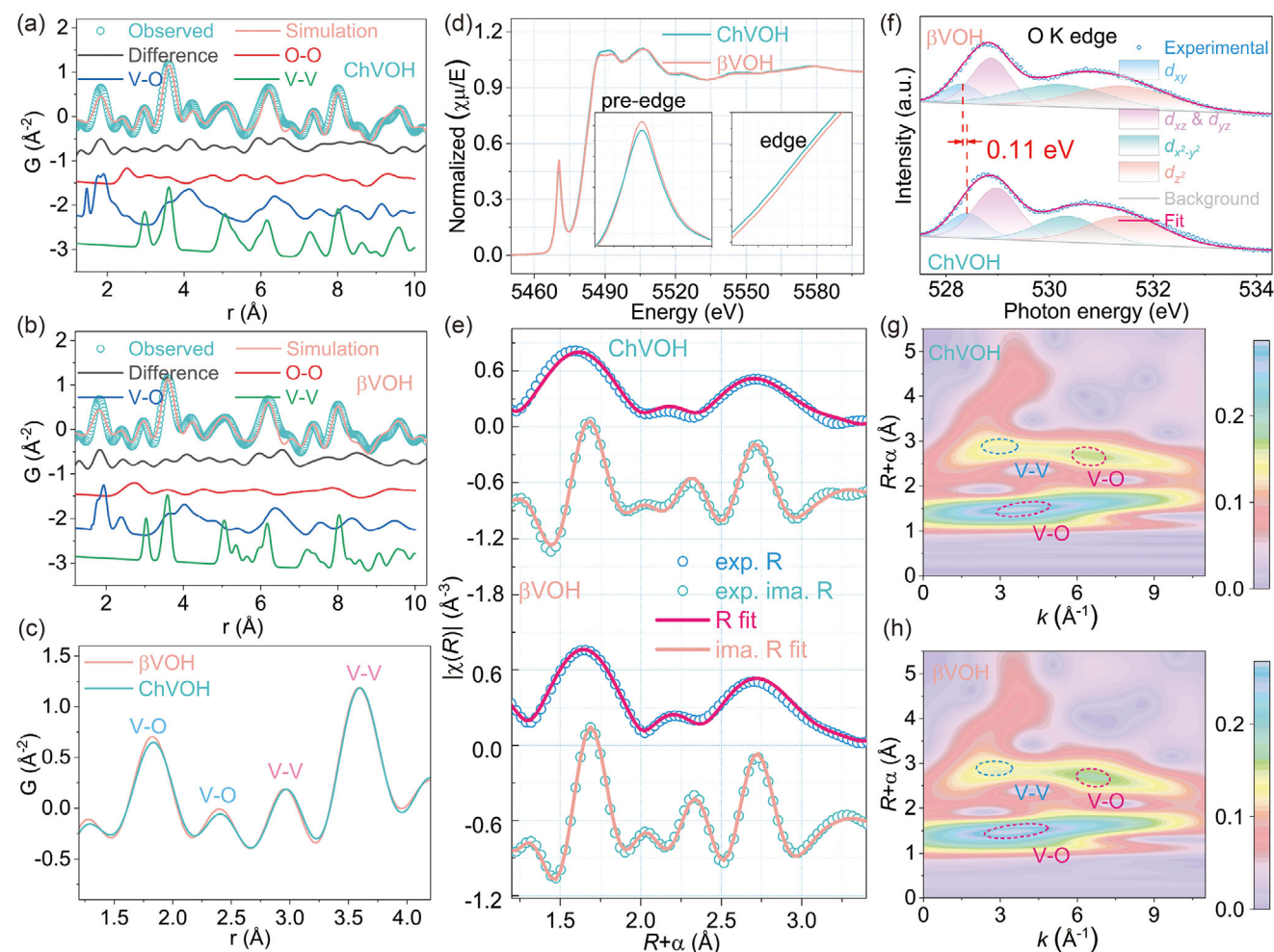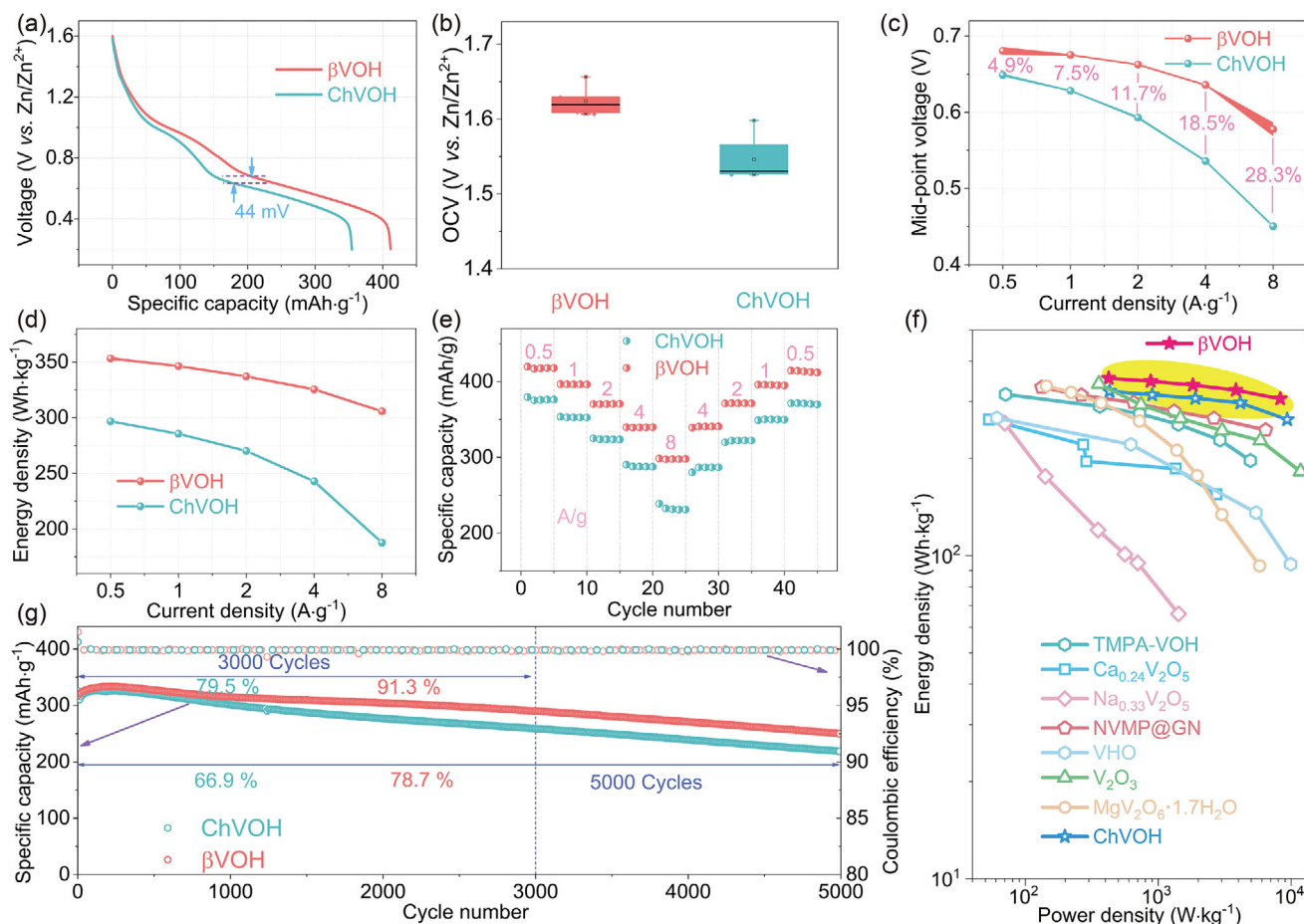
Figure 2. Coordination structure of the V atom. The experimental X-ray PDF data of a) ChVOH and b) βVOH fitted by the $V_2O_5 \cdot nH_2O$ model over the range of $1.2 < r < 10.3$ Å. The simulated partial PDF of the refined structural model is shown in the offset for each atomic pair. c) The comparison of X-ray PDF data for both samples. d) V K-edge XAFS spectra. The pre-edge peak reflects the octahedra distortion and the $1s \rightarrow 3d$ electron hopping, and the near-edge presents the chemical state of V in the different chemical surroundings. e) R-space spectra of ChVOH and βVOH from the K^2-weighted Fourier transform of the V K-edge EXAFS. f) O 1s X-ray absorption spectra of ChVOH and βVOH. Wavelet transform diagrams of g) ChVOH and h) βVOH.

prominent scattering peaks observed at ≈1.7 and 2.2 Å in both samples, which originate from single-scattering contributions of O atoms within the first coordination shell. Peaks ≈2.7 Å originate from the scattering contributions of V—V between adjacent octahedra. Detailed quantitative analysis of O coordination geometry and V—O bond length parameters is comprehensively documented in Figures S4–S6 and Tables S4 and S5 (Supporting Information). The pre-intercalated cations induce structural contraction of V—O bonds along the c-axis, subjecting the d_{z^2}, d_{xz}, and d_{yz} orbitals to enhanced electronic repulsion from ligand O that elevates their energy levels. Conversely, the $d_{x^2-y^2}$ and d_{xy} orbitals exhibit reduced energy levels due to diminished repulsive interactions along their respective spatial orientations. This subtle difference in energy level alignment drives secondary splitting of the V 3d orbitals. Furthermore, comparative structural analysis reveals a moderate expansion of [VO₆] octahedra in βVOH relative to ChVOH, consequently lowering the energy levels of the

V 3d orbitals – a phenomenon that will be quantitatively examined in subsequent electronic structure analysis. The O K-edge in soft X-ray X-ray absorption spectra (XAS) (Figure 2f) originates from dipole-allowed transitions between O 1s core levels and unoccupied states with significant O 2p orbitals hybridization in the conduction band. The prominent doublets ≈530–537 eV arise from crystal field splitting of V 3d orbitals into distinct electronic structures. The higher-energy component corresponds to the e_g orbitals oriented along the octahedral axes, which form strong directional σ-antibonding states through enhanced overlap with ligand O atoms. The lower-energy component arises from the t_{2g} orbitals exhibiting weaker π-antibonding character due to reduced orbital overlapping with ligand O atoms.[45] Notably, the t_{2g} states undergo secondary splitting induced by axial compression of [VO₆] octahedra along the c-axis direction.[46] The energy position of the d_{xy}-derived spectral feature is governed by the energy difference between O 1s core levels and hybridized O 2p/V

**ADVANCED
SCIENCE NEWS**

www.advancedsciencenews.com

**ADVANCED
FUNCTIONAL
MATERIALS**

www.afm-journal.de

Figure 3. Electrochemical performances of βVOH and ChVOH cathodes in rechargeable batteries. a) The GCD curves at 0.5 A g^{-1}. b) OCV statistics. c) Mid-point voltages and d) Energy densities of both samples collected at different current densities. e) Rate performance. The enhanced rate performance of βVOH is offered by the improved structural flexibility under high current density. f) Ragone plot on the active material level. The higher mid-point voltages benefit to offer higher energy densities in βVOH. g) Cycling stability at 8 A g^{-1} of both samples in the Zn-ion battery.

$3d$ unoccupied states in the conduction band.[47] Notably, this characteristic exhibits a marked low-energy shift ($\Delta E = 0.11$ eV) in βVOH compared to ChVOH, providing electronic-level validation for the structural distortion patterns revealed through R-space Fourier-transform analysis. In the corresponding wavelet transform spectra (Figure 2g,h), the predominant spectral features originate from V—O single-scattering contributions within the primary coordination sphere, which manifest at lower energy regimes due to the characteristic vibrational modes of O atoms. Subsequent spectral components are systematically assigned to V—V (secondary coordination sphere) and V—O (tertiary coordination sphere) multiple-scattering pathways, respectively.

2.3. Structure and Performance Correlation

The electrochemical performance of ChVOH and βVOH cathodes was assessed against zinc foil as the anode. Galvanostatic charge/discharge (GCD) measurements conducted at a current density of 0.5 A g^{-1} (**Figure 3**a) reveal that ChVOH exhibits distinct discharge plateaus in the voltage ranges of 1.1–0.8 V and

0.8–0.3 V, which correspond to the multistage Zn^{2+} intercalation processes. Notably, the elevated discharge voltage of βVOH compared to ChVOH can be attributed to the lower energy levels of $3d$ orbitals, as shown in Figure S7 (Supporting Information) and supported by EXAFS and soft XAS. As mentioned above, the [VO$_6$] octahedral units in βVOH undergo a slight expansion relative to those in ChVOH in EXAFS analysis. This structural modification induces a downward shift in the overall $3d$ orbital energy levels of βVOH, as evidenced by soft XAS data, which facilitates more energetically favorable redox reactions during electrochemical processes. At various current densities of 1, 2, 4, and 8 A g^{-1} (Figure S8, Supporting Information), βVOH demonstrates higher working voltages compared to ChVOH. This observation confirms the enhanced electrochemical performance of βVOH in terms of voltage elevation during discharge processes. Figure S9 (Supporting Information) presents a comparative analysis of the cyclic voltammetry (CV) profiles for both βVOH and ChVOH electrodes. Both materials exhibit a narrow potential interval between the anodic and cathodic peaks, which makes the redox more reversible.[48] EIS before and after three cycles of CV testing at 0.1 mV s^{-1} is shown in Figure S10 (Supporting

**ADVANCED
SCIENCE NEWS**

www.advancedsciencenews.com

**ADVANCED
FUNCTIONAL
MATERIALS**

www.afm-journal.de

Information). Compared with ChVOH, βVOH exhibits a lower charge transfer resistance (R_{ct}), indicating a higher charge transfer rate in βVOH. The significant decrease in the R_{ct} value after the CV test can be attributed to the activation of the electrodes, including the formation of lattice-trapped Zn^{2+}, enhancing the electrical conductivity and the penetration of electrolyte, boosting mass transfer.[49] The open-circuit voltage (OCV) of a rechargeable battery is generally defined as $V_{oc} = (\mu_A - \mu_C)/e$, where μ_A and μ_C represent the electrochemical potentials of the anode and cathode, respectively. For cathode materials, μ_C is intrinsically linked to the redox-active transition metal orbitals. XPS analysis reveals that ChVOH contains a higher concentration of V^{4+} species compared to βVOH, leading to increased electron occupancy in lower-energy d_{xy} orbitals. This electronic structure elevates μ_C in ChVOH, resulting in a reduced Voc relative to βVOH (Figure 3b). Consistent with this mechanism, βVOH demonstrates higher mid-point voltages than ChVOH (Figure 3c), a direct consequence of its reduced d-orbital energy levels as evidenced by spectroscopic and structural analyses. In Figure 3d, βVOH demonstrates a significantly higher energy density compared to ChVOH. This performance enhancement primarily originates from the elevated average working voltage and specific capacity of βVOH, achieved through modulation of local chemical coordination environments. Figure 3e demonstrates the rate performance comparison between βVOH and ChVOH through a stepwise current density variation protocol ($0.5 \rightarrow 8$ A g$^{-1} \rightarrow 0.5$ A g^{-1}). βVOH maintains 71.3% of its initial capacity (measured at 0.5 A g^{-1}) when cycled at 8 A g^{-1}, significantly outperforming ChVOH, which retains merely 60.8% capacity under identical high-current conditions. Remarkably, βVOH exhibits superior capacity recovery with 414.6 mA h g^{-1} restored upon returning to 0.5 A g^{-1}, demonstrating exceptional structural reversibility. This contributes to the higher energy efficiency of βVOH, as shown in Figure S11b (Supporting Information). The Ragone plot in Figure 3f provides a comprehensive comparison of specific energy versus specific power between our Zn//βVOH battery system and current aqueous zinc-ion batteries (ZIBs) reported in the literature. Notably, the Zn//βVOH battery exhibits exceptional energy storage capabilities, delivering a specific energy of 354.3 Wh kg^{-1} at a specific power of 423.7 W kg^{-1}, while maintaining 305.8 Wh kg^{-1} energy density even under ultrahigh power density at 8277.3 W kg^{-1} – all values calculated based on active material mass. These performances surpass those of previously reported cathode materials for ZIBs, including TMPA-VOH,[50] $Ca_{0.24}V_2O_5$,[51] $Na_{0.33}V_2O_5$,[52] NVMP@GN,[53] VHO,[30] V_2O_3,[54] and $MgV_2O_6 \cdot 1.7H_2O$.[55] The βVOH cathode demonstrates exceptional cycling stability in a Zn-ion battery at 8 A g^{-1}, as evidenced in Figure 3g. Electrochemical evaluation reveals a remarkable capacity retention of 91.3% after 3000 continuous charge–discharge cycles for βVOH, significantly outperforming the ChVOH counterpart, which shows 79.5% retention under identical testing conditions. This performance divergence can be attributed to superior electrochemical kinetics and enhanced structural integrity of βVOH during high-rate cycling. Galvanostatic intermittent titration technique (GITT) was employed to determine the Zn^{2+} diffusion coefficients in zinc-ion batteries for both samples (Figure S10a, Supporting Information). The calculated Zn^{2+} diffusion coefficients in βVOH demonstrate higher values than those in ChVOH, which accounts for the superior

rate performance. These findings demonstrate that modulation of the local coordination environment effectively enhances electrochemical performance.[56] Figure S12a (Supporting Information) presents the GCD profiles of lithium-ion batteries employing βVOH and ChVOH as cathode materials at a current density of 0.01 A g^{-1}. The discharge voltage plateau corresponding to the $V^{5+} \rightarrow V^{4+}$ redox transition in βVOH exhibits a substantial elevation compared to that observed in ChVOH. This voltage enhancement phenomenon persists in sodium-ion battery systems, where βVOH demonstrates superior discharge voltage relative to ChVOH at 0.02 A g^{-1} (Figure S12b, Supporting Information). These findings collectively confirm the feasibility of optimizing working voltage through regulation of local atomic structures and crystal field effects in vanadium oxide-based electrode materials.

DFT calculations are performed to further investigate the detailed crystal structures and density of states (DOS) of both samples. DOS in **Figure 4a,b** suggest that the conduction bands are attributed to V 3d, while O 2p highly contributes to the valence bands. For both samples, the Fermi levels sit across the conduction bands, contributing to high electrical conductivities. Compared with ChVOH, an additional electronic state of βVOH more to the Fermi level, which is conducive to electron transfer, benefiting to improve the comprehensive electrochemical performance.[57,58,18] The orbital hybridization diagram of both samples is displayed in Figure 4c.[59] The elongated V—O bond lengths within the [VO_6] octahedral units of βVOH, as experimentally confirmed by EXAFS and PDF analyses in contrast to ChVOH, effectively mitigate electron–electron repulsion between O 2p and V 3d orbitals,[60] inducing a downward energy shift in the hybrid molecular orbitals formed through V 3d and O 2p orbital interactions within the βVOH relative to ChVOH. This electronic stabilization is predominantly evidenced by two distinctive features in the βVOH electronic structure: the V d-band center in βVOH undergoes a downward shift in energy relative to ChVOH, and βVOH possesses a greater number of unoccupied 3d orbitals. The synergistic interaction of these factors collectively enhances the stabilization energy of hybrid orbitals in the βVOH, thereby accounting for the higher working voltage and enhanced structural stability observed in βVOH compared to ChVOH. Ex situ XRD characterization (Figure 4d,e) provides a mechanistic understanding of Zn^{2+} intercalation/deintercalation dynamics and associated structural evolutions in both samples. The structural reversibility is evidenced by systematic variations in (001) and (002) diffraction features during electrochemical cycling. In the full discharge state, βVOH demonstrates superior structural retention compared to ChVOH, as manifested by reduced peak shift of the (001) diffraction peak ($\Delta 2\theta = 0.71°$ vs 0.84° for ChVOH), and the (001) diffraction peak of βVOH persists under the fully discharge state, whereas that of ChVOH is not observed under identical conditions. These observations directly correlate with enhanced cycling stability and rate performance of βVOH, particularly indicating the robust structural integrity during repeated ion insertion/extraction cycles. This phenomenon can be attributed to the lower-energy hybrid molecular orbital structures of βVOH, enhanced stability of electron occupancy, and the shielding effects of the more stable N—O bonds on the Zn^{2+} and O^{2-} interactions.[36] As shown in Figure 4f, the interplanar spacing of pre-intercalated ChVOH is 12.9 Å, exceeding the 12.6 Å observed in βVOH. During the discharge process, the
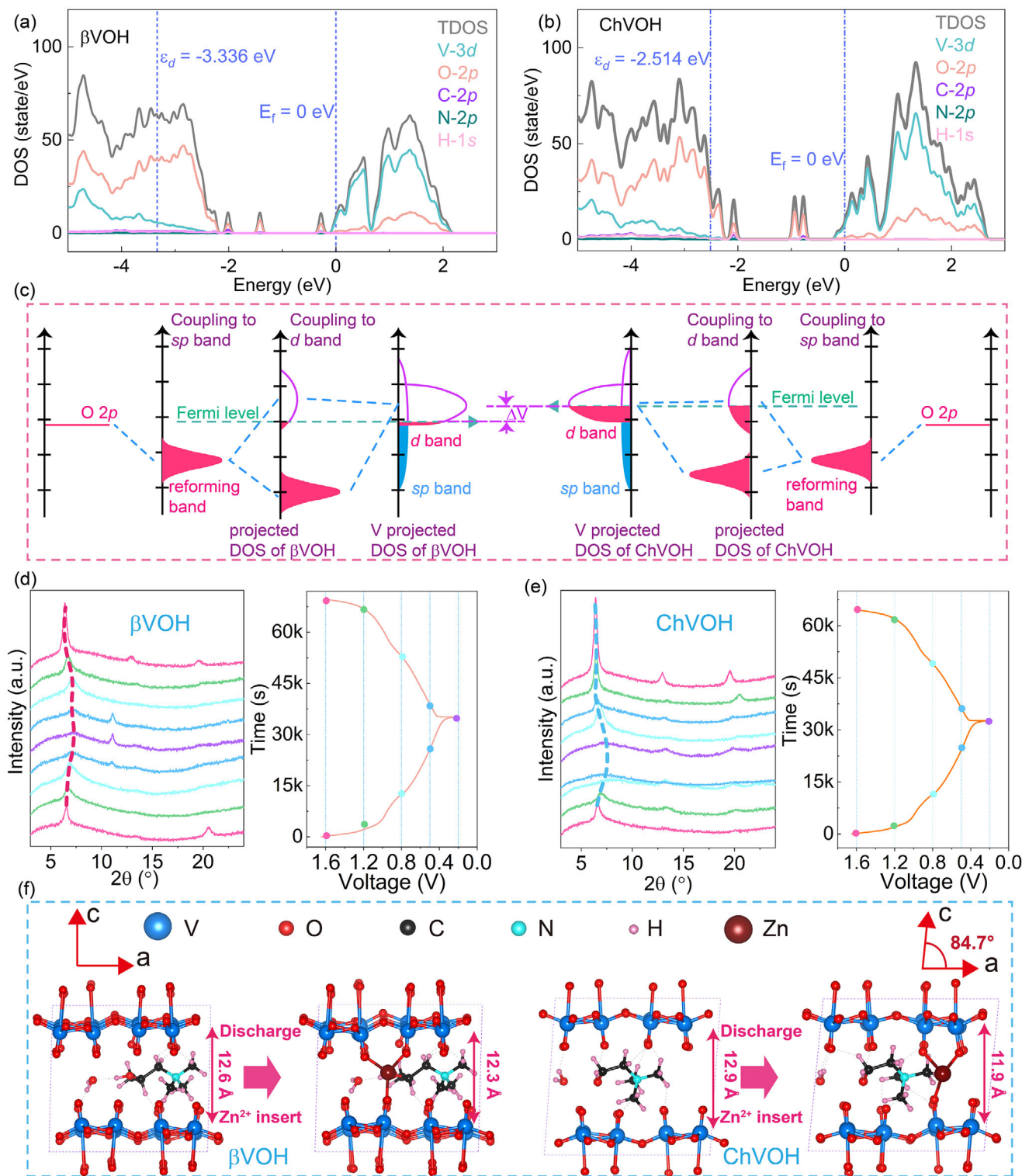
Figure 4. Structures and energy levels of ChVOH and βVOH. DOS of a) βVOH and d) ChVOH. The energy level of the d-band center in βVOH shifts to a lower energy position compared to that in ChVOH. c) The orbitals hybridization diagram of βVOH and ChVOH, the hybridized molecular orbital energy levels formed by the interaction between V $3d$ and O $2p$ orbitals exhibit a lower energy level in βVOH compared to ChVOH. d,e) Structural evolution characterized by ex situ XRD. Ex situ XRD measurements accompanied by GCD profiles at the current density of 0.5A g^{-1} for the first cycle between 0.2 and 1.6 V for (d) βVOH and (e) ChVOH. f) The calculated crystal structural evolution of βVOH and ChVOH during Zn^{2+} (de)intercalation processes.

**ADVANCED
SCIENCE NEWS**

www.advancedsciencenews.com

**ADVANCED
FUNCTIONAL
MATERIALS**

www.afm-journal.de

ChVOH lattice undergoes a contraction of 1.0 Å, in contrast to the 0.3 Å contraction observed in βVOH. These structural changes align well with the corresponding ex situ XRD analysis results, thereby confirming the superior structural stability of βVOH.

3. Conclusion

The integration of electronic structure evolution analysis and electrochemical energy storage performance evaluation in samples with local structural distortions provides valuable insights for achieving enhanced working voltage and improved cycling stability. By controlling the distortions of $[VO_6]$ octahedra, it is possible to precisely modulate the crystal field environment, effectively lowering the energy states of V $3d$ orbitals. This optimization yields a substantial elevation in mid-point working voltage alongside improved cyclability in the locally-engineered βVOH. These results demonstrate a universal strategy of crystal field engineering through geometric distortion control in transition metal oxide electrodes. In addition, the βVOH cathode exhibits remarkably high energy density and superior cycling stability, demonstrating a capacity retention rate of 91.3% after 3000 cycles in zinc-ion batteries. These results not only reveal the structural origins of energy level evolution but also provide fundamental design principles for enhancing both working voltage and crystal stability through precise modulation of local coordination environments for next-generation rechargeable batteries.

Supporting Information

Supporting Information is available from the Wiley Online Library or from the author.

Acknowledgements

Conflict of Interest

The authors declare no conflict of interest.

Data Availability Statement

The data that support the findings of this study are available from the corresponding author upon reasonable request.

Keywords

[1] Y. Liang, Y. Yao, *Nat. Rev. Mater.* **2022**, *8*, 109.

[2] Y. Liang, H. Dong, D. Aurbach, Y. Yao, *Nat. Energy* **2020**, *5*, 646.

[3] M. Li, Z. Li, X. Wang, J. Meng, X. Liu, B. Wu, C. Han, L. Mai, *Energy Environ. Sci.* **2021**, *14*, 3796.

[4] M.-H. Kim, H. Jang, E. Lee, J. Seo, J. Park, A. Choi, T. Kim, M. Choi, E. Kim, Y. H. Jung, S. J. Kang, J. Cho, Y. Li, M. G. Kim, D.-H. Seo, H.-W. Lee, *Sci. Adv.* **2025**, *11*, adt0232.

[5] H. Liu, L. Yang, T. Shen, C. Li, T. Kang, H. Niu, W.-H. Huang, C.-C. Chang, M. Yang, G. Cao, C. Liu, *ACS Nano* **2025**, *19*, 9132.

[6] H. Park, H. Park, K. Song, S. H. Song, S. Kang, K.-H. Ko, D. Eum, D. Jeon, J. Kim, W. M. Seong, H. Kim, J. Park, K. Kang, *Nat. Chem.* **2022**, *14*, 614.

[7] S. Chen, D. Ji, Q. Chen, J. Ma, S. Hou, J. Zhang, *Nat. Commun.* **2023**, *14*, 3526.

[8] D. Kundu, B. D. Adams, V. Duffort, S. H. Vajargah, L. F. Nazar, *Nat. Energy* **2016**, *1*, 16119.

[9] J. Yao, Y. Li, R. C. Massé, E. Uchaker, G. Cao, *Energy Storage Mater.* **2018**, *11*, 205.

[10] M. Yan, P. He, Y. Chen, S. Wang, Q. Wei, K. Zhao, X. Xu, Q. An, Y. Shuang, Y. Shao, K. T. Mueller, L. Mai, J. Liu, J. Yang, *Adv. Mater.* **2017**, *30*, 1703725.

[11] S. K. Park, W. M. Dose, B. D. Boruah, M. De Volder, *Adv. Mater. Technol.* **2021**, *7*, 2100799.

[12] M. Song, H. Tan, D. Chao, H. J. Fan, *Adv. Funct. Mater.* **2018**, *28*, 1802564.

[13] J. Guo, B. He, W. Gong, S. Xu, P. Xue, C. Li, Y. Sun, C. Wang, L. Wei, Q. Zhang, Q. Li, *Adv. Mater.* **2023**, *36*, 2303906.

[14] Y. Liu, C. Lu, Y. Yang, W. Chen, F. Ye, H. Dong, Y. Wu, R. Ma, L. Hu, *Adv. Mater.* **2024**, *36*, 2312982.

[15] L. Hu, Z. Wu, C. Lu, F. Ye, Q. Liu, Z. Sun, *Energy Environ. Sci.* **2021**, *14*, 4095.

[16] Y. Zhang, Q. Li, W. Feng, H. Yue, S. Gao, Y. Su, Y. Tang, J. Wu, Z. Zhang, Y. Zhang, M. Shakouri, H. Chen, H. Pang, *Angew. Chem., Int. Ed.* **2025**, *64*, 202501728.

[17] S. Liu, H. Zhu, B. Zhang, G. Li, H. Zhu, Y. Ren, H. Geng, Y. Yang, Q. Liu, C. C. Li, *Adv. Mater.* **2020**, *32*, 2001113.

[18] Q. Sun, H. Cheng, Y. Yuan, Y. Liu, W. Nie, K. Zhao, K. Wang, W. Yao, X. Lu, J. Lu, *Adv. Energy Mater.* **2022**, *13*, 2202515.

[19] C. Liu, Z. Neale, J. Zheng, X. Jia, J. Huang, M. Yan, M. Tian, M. Wang, J. Yang, G. Cao, *Energy Environ. Sci.* **2019**, *12*, 2273.

[20] X. Chen, H. Zhang, J.-H. Liu, Y. Gao, X. Cao, C. Zhan, Y. Wang, S. Wang, S.-L. Chou, S.-X. Dou, D. Cao, *Energy Storage Mater.* **2022**, *50*, 21.

[21] R. Li, F. Xing, T. Li, H. Zhang, J. Yan, Q. Zheng, X. Li, *Energy Storage Mater.* **2021**, *38*, 590.

[22] H. Liu, H. Niu, W.-H. Huang, T. Shen, C. Li, C.-C. Chang, M. Yang, C. Gao, L. Yang, Q. Zong, Y. Pei, G. Cao, C. Liu, *ACS Energy Lett.* **2024**, *9*, 5492.

[23] X. Jia, C. Liu, Z. Wang, D. Huang, G. Cao, *Nano-Micro Lett.* **2024**, *16*, 129.

[24] Q. Zong, Y. Zhuang, C. Liu, Q. Kang, Y. Wu, J. Zhang, J. Wang, D. Tao, Q. Zhang, G. Cao, *Adv. Energy Mater.* **2023**, *13*, 2301480.

[25] J. Wang, J. Wang, Y. Jiang, F. Xiong, S. Tan, F. Qiao, J. Chen, Q. An, L. Mai, *Adv. Funct. Mater.* **2022**, *32*, 2113030.

[26] B. Wang, S. Dai, Z. Zhu, L. Hu, Z. Su, Y. Jin, L. Xiong, J. Gao, J. Wan, Z. Li, L. Huang, *Nanoscale* **2022**, *14*, 12013.

[27] E. Ruiz-Hitzky, B. Casal, *J. Chem. Soc.* **1986**, *82*, 1597.

[28] J. H. Park, K. W. Oh, H.-M. Choi, *Cellulose* **2013**, *20*, 2101.

**ADVANCED
SCIENCE NEWS**

www.advancedsciencenews.com

**ADVANCED
FUNCTIONAL
MATERIALS**

www.afm-journal.de

[29] S. Shi, M. Cao, X. He, H. Xie, *Cryst. Growth Des.* **2007**, *7*, 1893.

[30] S. Zhang, Z. Zou, Y. Gao, J. Geng, M. Chen, W. Ling, F. Liang, X. Peng, M. Zhou, F. Yu, S. Jia, *Nano Energy* **2023**, *115*, 108736.

[31] G. A. Sawatzky, D. Post, *Phys. Rev. B* **1979**, *20*, 1546.

[32] V. Bondarenka, S. Grebinskij, S. Kaciulis, G. Mattogno, H. T. S. Mickevicius, V. Volkov, G. Zakharova, *J. Electron. Spectrosc. Relat. Phenom.* **2001**, *120*, 131.

[33] Q. Wang, Q. Feng, Y. Lei, S. Tang, L. Xu, Y. Xiong, G. Fang, Y. Wang, P. Yang, J. Liu, W. Liu, X. Xiong, *Nat. Commun.* **2022**, *13*, 3689.

[34] T. Egami, S. J. L. Billinge, *Underneath the Bragg Peaks: Structural Analysis of Complex Materials*, 2nd Edition, Elsevier, Amsterdam, Netherlands **2012**.

[35] S. J. L. Billinge, S. H. Skjaervoe, M. W. Terban, S. Tao, L. Yang, Y. Rakita, B. A. Frandsen, *Comprehensive Inorganic Chemistry III*, 2nd Edition, (Eds: J. Reedijk, K. R. Poeppelmeier), Elsevier, Amsterdam, Netherlands **2023**, 222.

[36] H. Niu, H. Liu, L. Yang, T. Kang, T. Shen, B. Jiang, W.-H. Huang, C.-C. Chang, Y. Pei, G. Cao, C. Liu, *Nat. Commun.* **2024**, *15*, 9421.

[37] P. J. Chupas, X. Qiu, J. C. Hanson, P. L. Lee, C. P. Grey, S. J. L. Billinge, *J. Appl. Crystallogr.* **2003**, *36*, 1342.

[38] C. L. Farrow, P. Juhas, J. W. Liu, D. Bryndin, E. S. Božin, J. Bloch, T. Proffen, S. J. L. Billinge, *J. Phys.: Condens. Matter* **2007**, *19*, 335219.

[39] P. Juhás, T. Davis, C. L. Farrow, S. J. L. Billinge, *J. Appl. Crystallogr.* **2013**, *46*, 560.

[40] Y. Su, J. Hu, G. Yuan, G. Zhang, W. Wei, Y. Sun, X. Zhang, Z. Liu, N. Suen, H. Chen, H. Pang, *Adv. Mater.* **2023**, *35*, 2307003.

[41] R. Sarangi, *Coord. Chem. Rev.* **2013**, *257*, 459.

[42] T. E. Westre, P. Kennepohl, J. G. DeWitt, B. Hedman, K. O. Hodgson, E. I. Solomon, *J. Am. Chem. Soc.* **1997**, *119*, 6297.

[43] R. G. Shulman, Y. Yafet, P. Eisenberger, W. E. Blumberg, *Proc. Natl. Acad. Sci. USA* **1976**, *73*, 1384.

[44] B. Ravel, M. Newville, *J. Synchrotron Radiat.* **2005**, *12*, 537.

[45] M. Abbate, H. Pen, M. T. Czyiyk, F. M. F. d. Groat, J.-C. Fuggleav, Y. J. Mab, C. T. Chenb, F. Setteb, A. Fujimori, Y. Uedad, K. Kosugee, *J. Electron. Spectrosc. Relat. Phenom.* **1993**, *62*, 185.

[46] Y. Wang, S. Wei, Z. H. Qi, S. Chen, K. Zhu, H. Ding, Y. Cao, Q. Zhou, C. Wang, P. Zhang, X. Guo, X. Yang, X. Wu, L. Song, *Proc. Natl. Acad. Sci. USA* **2023**, *120*, 2217208120.

[47] D. W. Fischer, *J. Appl. Phys.* **1970**, *41*, 3561.

[48] Q. Tan, X. Li, B. Zhang, X. Chen, Y. Tian, H. Wan, L. Zhang, L. Miao, C. Wang, Y. Gan, J. Jiang, Y. Wang, H. Wang, *Adv. Energy Mater.* **2020**, *10*, 2001050.

[49] C. Liu, Z. Neale, J. Zheng, X. Jia, J. Huang, M. Yan, M. Tian, M. Wang, J. Yang, G. Cao, *Energy Environ. Sci.* **2019**, *12*, 2273.

[50] X. Jia, C. Liu, Z. Wang, D. Huang, G. Cao, *Nano-Micro Lett.* **2024**, *16*, 129.

[51] C. Xia, J. Guo, P. Li, X. Zhang, H. N. Alshareef, *Angew. Chem., Int. Ed.* **2018**, *57*, 3943.

[52] P. He, G. Zhang, X. Liao, M. Yan, X. Xu, Q. An, J. Liu, L. Mai, *Adv. Energy Mater.* **2018**, *8*, 1702463.

[53] Z. Wu, F. Ye, Q. Liu, R. Pang, Y. Liu, L. Jiang, Z. Tang, L. Hu, *Adv. Energy Mater.* **2022**, *12*, 2200654.

[54] J. Ding, H. Zheng, H. Gao, Q. Liu, Z. Hu, L. Han, S. Wang, S. Wu, S. Fang, S. Chou, *Adv. Energy Mater.* **2021**, *11*, 2100973.

[55] X. Wang, Z. Zhang, S. Xiong, F. Tian, Z. Feng, Y. Jia, J. Feng, B. Xi, *Small* **2021**, *17*, 2100318.

[56] Y. Liu, J. Xu, J. Li, Z. Yang, C. Huang, H. Yu, L. Zhang, J. Shu, *Coord. Chem. Rev.* **2022**, *460*, 214477.

[57] Q. Zang, X. Cheng, S. Chen, Z. Xiao, K.-P. Wang, L. Zong, Q. Zhang, L. Wang, *Chem. Eng. J.* **2023**, *452*, 139396.

[58] X. Cheng, Z. Xiang, C. Yang, Y. Li, L. Wang, Q. Zhang, *Adv. Funct. Mater.* **2024**, *34*, 2311412.

[59] J. K. Nørskov, F. Abild-Pedersen, F. Studt, T. Bligaard, *Proc. Natl. Acad. Sci. USA* **2011**, *108*, 937.

[60] Z. Hou, J. Wang, N. Dai, S. Yao, S. Wang, Y. Ji, X. Gao, H. Zhang, Z. Tang, Y. Sun, S. Li, Y. Liu, W. Fu, K. Nie, Y. Jiang, Y. M. Yan, Z. Yang, *Adv. Energy Mater.* **2023**, *14*, 2302477.